Plasma Science and
Technology

ACCEPTED MANUSCRIPT

Interaction of dynamic magnetic island with bootstrap current in toroidal plasma

To cite this article before publication: Wenjin Chen *et al* 2025 *Plasma Sci. Technol.* in press https://doi.org/10.1088/2058-6272/adac91

Interaction of dynamic magnetic island with bootstrap current in toroidal plasma

Wenjin CHEN (陈文锦)[1,2], Min ZHANG (张敏)[1] and Zhiwei MA (马志为)[1,*]

[1] Institute for Fusion Theory and Simulation, Zhejiang University, Hangzhou 310027, People's Republic of China

[2] Southwestern Institute of Physics, Chengdu 610041, People's Republic of China

[*] E-mail of corresponding author: zwma@zju.edu.cn

Abstract

Interaction of dynamic magnetic island with bootstrap current in toroidal plasmas is investigated based on the first principles of kinetic simulation. The perturbed magnetic and electric fields associated with the dynamic magnetic island are calculated from a three-dimensional toroidal MHD code (CLT), instead of artificial imposed magnetic island perturbation. Inside the static magnetic island, the bootstrap current decreases as expected with the effective collision frequency. The radial electric field $\boldsymbol{E}_r$ associated with dynamic island could cause the $\boldsymbol{E}\times\boldsymbol{B}$ drift, which can noticeably modify the bootstrap current distribution. If the bootstrap current turns on when the tearing mode saturates, the widths of magnetic islands ascend rapidly and saturate again for both static and dynamic cases. But the saturated island width of the dynamic case is smaller than that of the static case because the magnetic islands in the dynamic case rotate due to strong asymmetric distribution of the bootstrap current in the vicinity of the X-points.

Keywords: bootstrap current, kinetic simulation, magnetic island, tokamak

(Some figures may appear in colour only in the online journal)

1. Introduction

Tearing mode (TM) instability causes a topologic change of magnetic field in a rational surface to form magnetic island structures in a tokamak. The fast parallel

diffusion along magnetic field lines causes flattening in the temperature, density, or pressure profiles inside magnetic islands. The reduction of bootstrap currents inside magnetic islands resulting from flattening the plasma pressure will boost the development of the tearing mode, which is called as the neoclassical tearing mode (NTM)[1–3]. NTM not only constrains the maximum achievable plasma beta but also triggers disruptions in tokamak plasma discharges. NTM instabilities typically arise in high-performance plasma discharges characterized by elevated plasma beta values, making them a significant concern for devices like ITER operating in H-mode scenarios [4, 5].

The dynamics of TM and NTM involve numerous physical processes across different spatial and temporal scales, including magnetic island dynamics linked to the curvature [6], the plasma beta [7], turbulence [8], and energetic particles [9, 10]. Recent simulations have focused on investigating NTM physics, exploring thresholds for the size of a seed island [11, 12] and an island saturation [13]. Also, the seed islands for the excitation of NTMs can be provided by the plasma perturbations from the core and/or boundary regions of tokamaks [14]. Controlling NTM in high β_N plasmas is therefore crucial for tokamak operation. For instance, applying an RF-current at the rational surface where the instability occurs has been proposed [15]. In MHD numerical investigations of NTM [16] or double neoclassical tearing mode (DNTM) [17], the bootstrap current in the Ohm's law is derived from the fluid model with an average over the flux surface $j_{bs} = \langle \boldsymbol{B} \cdot \boldsymbol{J} \rangle_{bs} = -f\left(\sqrt{\varepsilon}/B_\theta\right)\partial p/\partial r$. It is assumed that the island width W is much larger than the particle banana width w_b. Therefore, the bootstrap current completely vanishes inside a magnetic island. However, during the early phase of an NTM, when the seed island size W is comparable to the particle banana width ($W \approx w_b$) or ion poloidal Larmor radius ($W \approx \rho_{\theta i}$), kinetic simulations suggest that the orbits of charged particles, especially ions, in the region around the island could partially overlap the island and provide the source of the pressure gradient

inside the island. Therefore, a significant fraction of the bootstrap current survives within the island [18] and the pressure gradient is maintained across the magnetic island, which leads to a lower growth rate of NTM due to survival of the bootstrap current [19].

δ*f* Monte Carlo calculations have been employed to study neoclassical transport and the bootstrap current [20–23]. Poli *et al* [18, 24] observed that a substantial portion of the ion bootstrap current can persist within the island when the width of the trapped ion banana orbit w_b approaches the island width. If the island is too small $w_b/W \geq 1$, the drift orbits of passing ions can locate inside or outside the island. Therefore, the profiles of the ion density gradient and the bootstrap current almost remain unchanged. Wang *et al* investigated the recovery of ion density gradients inside islands under various collision regimes [25]. They suggested that the pressure gradient recovery, rather than finite banana-orbit effects, may play a pivotal role in maintaining the ion bootstrap current during NTM. However, the impact of magnetic islands on electron density gradients and electron bootstrap currents is more pronounced due to the smaller banana-orbit widths of electrons. In the presence of a magnetic island, the electron bootstrap current remains largely unaffected in the banana regime but is completely suppressed in the plateau region, with a small but finite bootstrap current existing inside the islands in the collisional regime. Additionally, a steeper electron density gradient at the island separatrix leads to a higher electron bootstrap current [26].

Previous bootstrap current simulations based on the δ*f* Monte Carlo method only considered static and artificially imposed magnetic island perturbations in the form of $\delta \boldsymbol{B} = \nabla \times \alpha \cos\xi \boldsymbol{B}_0$, where $\boldsymbol{B}_0$ is the equilibrium magnetic field, α represents the strength of the perturbation, and ξ is the helical angle [18, 24–26]. However, during the evolution of the (neoclassical) tearing mode, the magnetic island evolves over time, inducing an electric field $\boldsymbol{E}$ through magnetic reconnection. The parallel component of the electric field $\boldsymbol{E}_{//} = (\boldsymbol{E} \cdot \boldsymbol{b})\boldsymbol{b}$ responds to plasma acceleration or deceleration along flux surfaces, where $\boldsymbol{b} = \boldsymbol{B}/B$ is the unit vector along the field line. Moreover, as magnetic

field lines become stochastic, electrons are lost along these lines while ions are trapped, resulting in a strong radial electric field $\boldsymbol{E}_r$ [27]. This radial electric field $\boldsymbol{E}_r$ can influence the drift displacements and orbits of charged particles [28]. Furthermore, during the time evolution of NTM, the island rotates with plasma flow, but the polarization effect associated with rotating magnetic islands due to plasma flow has not been studied in this paper, though it remains a topic for future investigation.

The objective of this study is to develop a kinetic-magnetohydrodynamics (MHD) hybrid simulation of NTM dynamics. Specifically, this simulation is akin to particle/MHD hybrid models such as M3D-K [29], MEGA [30], or CLT-K [31], which describe the interaction between energetic particles and MHD phenomena. The energetic particle effects enter through the particle pressure tensor in the momentum equation. In this simulation, the bootstrap current ($\boldsymbol{J}_{\mathrm{bs}}$) is calculated using gyro-center approximation particles and is incorporated into the MHD code (CLT code) through Ohm's law to investigate crucial NTM dynamics, as illustrated in figure 1. Unlike the fluid model $j_{\mathrm{bs}} = -f\left(\sqrt{\varepsilon}/B_\theta\right)\partial p/\partial r$, the bootstrap current is calculated in the kinetic model without averaging over flux surfaces.

In this paper, we present our results about the interaction of dynamic magnetic island perturbation with the bootstrap current. The perturbed magnetic $\delta\boldsymbol{B}$ and electric fields $\boldsymbol{E}$ associated with the dynamic magnetic island are calculated from a three-dimensional toroidal MHD code (CLT), instead of artificial imposed magnetic island perturbation. The dynamics of magnetic islands induce an electric field which includes the parallel electric field $\boldsymbol{E}_{//}$ and the radial electric field $\boldsymbol{E}_r$. The bootstrap current is mainly affected by the radial electric field $\boldsymbol{E}_r$ rather than the parallel electric field $\boldsymbol{E}_{//}$ because $\boldsymbol{E}_r$ is far larger than $\boldsymbol{E}_{//}$. The radial electric field $\boldsymbol{E}_r$ could cause the $\boldsymbol{E}\times\boldsymbol{B}$ drift. Consequently, electrons accumulate near the X point of islands, which can noticeably modify the electron bootstrap current. The redistributed dynamic bootstrap current changes the magnetic topology. This results in magnetic islands rotating.

The paper is organized as follows. Section 2 presents the formulation and

verification of the neoclassical simulation scheme. Section 3 discusses the flattened density within magnetic islands, the bootstrap current in static and dynamic magnetic islands, and the response of magnetic islands to the bootstrap current. The conclusion is provided in section 4.

2. Formulation and verification of neoclassical simulation

Our primary focus in this study is the investigation of the bootstrap current within dynamic magnetic islands. We adopt a cylindrical coordinate system (R, ϕ, Z) and compute the perturbed magnetic and electric fields associated with the dynamic magnetic island using the CLT code [32, 33]. Specifically, we consider an equilibrium with $q = 2$ to analyze the tearing mode instability with $m/n = 2/1$ islands, a critical aspect observed in tokamak experiments.

2.1. δ*f* Monte Carlo method for bootstrap current with dynamic magnetic islands

In the guiding-center phase space ($\boldsymbol{X}$, $v_{//}$), where $\boldsymbol{X}$ represents the guiding-center position and $v_{//} = \boldsymbol{b}\cdot\dot{\boldsymbol{X}}$ denotes the guiding-center parallel velocity, the kinetic equations governing the guiding-center distribution function f with a dynamic magnetic island take the following form [34]:

$$\begin{aligned}
&\frac{\mathrm{d}f}{\mathrm{d}t} = \frac{\partial f}{\partial t} + \dot{\boldsymbol{X}}\cdot\nabla f + \dot{v}_{//}\frac{\partial f}{\partial v_{//}} - C(f) = 0 \\
&\frac{\mathrm{d}\boldsymbol{X}}{\mathrm{d}t} = \frac{1}{B^*_{//}}\left(v_{//}\boldsymbol{B}^* + \boldsymbol{E}^*\times\boldsymbol{b}\right) \\
&\frac{\mathrm{d}v_{//}}{\mathrm{d}t} = \frac{Ze}{mB^*_{//}}\boldsymbol{B}^*\cdot\boldsymbol{E}^*
\end{aligned} \tag{1}$$

where $B^*_{//} = \boldsymbol{b}\cdot\boldsymbol{B}^*$ signifies the effective magnetic field $\boldsymbol{B}^*$ in the parallel direction, and $\boldsymbol{E}^*$ denotes the effective electric field (see Appendix A). The electromagnetic fields associated with the dynamic magnetic islands are derived from the CLT code. The distribution function f is decomposed into a time-independent equilibrium part f_0 and a perturbed part δf, with a local Maxwellian distribution considered for the equilibrium

$f_0 = n_0(\boldsymbol{X})\, f_M$. In our simulations, we assumed that the ion temperature is much smaller than the electron temperature $T_i \ll T_e$ and the quasi-neutrality is always satisfied $n_i \approx n_e$, then $p_i \ll p_e$ in the kinetic model. Thus, the bootstrap current is contributed solely by electrons located within an annular section of the torus. We employ a weighting scheme for the δf method of kinetic particle simulation [20], where the particle weight $w = \delta f/f$ is expressed as:

$$\frac{\mathrm{d}w}{\mathrm{d}t} = -(1-w)\left(\frac{v_{//}^2 \nabla \times \boldsymbol{b}_0}{\Omega} + \frac{\mu \boldsymbol{b}_0 \times \nabla B_0}{m_e \Omega} + v_{//}\frac{\delta \boldsymbol{B}}{B_0} + \frac{\boldsymbol{E} \times \boldsymbol{b}}{B}\right) \cdot \boldsymbol{\kappa} \quad (2)$$

where $\boldsymbol{\kappa} = \nabla n_0/n_0 + (E/T_0 - 3/2)\nabla T_0/T_0$ is associated with the scale parameters of the equilibrium gradients, $\Omega = ZeB/m_e$ represents the electron gyrofrequency, and the terms within the brackets on the right-hand side (RHS) of equation (2) correspond to the neoclassical drift velocity components, including the magnetic curvature and gradient drifts, the guiding center velocity due to magnetic flutter drive, and the $\boldsymbol{E}\times\boldsymbol{B}$ drift velocity. The perturbed electric field $\boldsymbol{E}$ induced by magnetic reconnections is self-consistently included in the kinetic mode in the dynamics island case.

We track a large number of electrons (nearly a total of 6×10^5 electrons) distributed throughout the torus. The initial guiding-center positions ($\boldsymbol{X}$) of the electrons are randomly determined to ensure uniform distribution in the poloidal and toroidal spaces. Electrons leaving the torus boundary are recycled to maintain a constant total particle number. The initial velocity of each electron is Maxwellian distributed within $-1.5v_{th} < v < 1.5v_{th}$. Following initialization, the guiding-center motions of electrons are determined by solving the Hamiltonian equations of motion (equation (1)) using a fourth-order Runge-Kutta algorithm during the orbit step. Subsequently, the guiding-center position ($\boldsymbol{X}$), parallel velocity ($v_{//}$), and weight w of electrons are updated using equation (1) and (2). In the collision step, the collision operator is simulated by updating the electron pitch angle $\lambda = v_{//}/v$ using the Monte Carlo pitch angle scattering model

of the Lorentz collision operator [20, 35]:

$$\lambda_{\text{new}} = \lambda_{\text{old}}\left(1-\nu_{\text{c}}\Delta t\right)+\left(R-0.5\right)\left[12\left(1-\lambda_{\text{old}}^2\right)\nu_{\text{c}}\Delta t\right]^{1/2} \tag{3}$$

where Δt represents the time step size, v_c is the collisional frequency. The effects of the Lorentz scattering operator will be reproduced if $v_c\Delta t << 1$. R is a uniformly distributed random number between 0 and 1, λ_{old} and λ_{new} denote the pitch angles after and before collision, respectively. With the specified marker weight $w = \delta f/f$, the parallel current density is given by [20]:

$$J_{\parallel} = \int \mathrm{d}v^3\left(ev_{//}\delta f\ B/B_0\right) = \sum_{i=1}^{N} ev_{//}w_i\delta\left(\boldsymbol{X}-\boldsymbol{X}_{\text{i}}\right)B/B_0 \tag{4}$$

where e represents the electron charge. It's important to note that this parallel current includes both the Pfirsch-Schlüter current (J_{ps}) and the bootstrap current (J_{bs}). The Pfirsch-Schlüter current ($J_{\text{ps}} = J_{\parallel}$) can be calculated in a collisionless process (see Appendix B) [36]. Therefore, the bootstrap current density is given by $J_{\text{bs}} = J_{\parallel} - J_{\text{ps}}$ in a collisional process. The bootstrap current density J_{bs} has been incorporated into Ohm's law. The full set of resistive MHD equations is as follows [32, 33]:

$$\begin{aligned}
&\frac{\partial\rho}{\partial t} = -\nabla\cdot(\rho\boldsymbol{v}) + \nabla\cdot[D\nabla(\rho-\rho_0)]\\
&\frac{\partial p}{\partial t} = -\boldsymbol{v}\cdot\nabla p - \Gamma p\nabla\cdot\boldsymbol{v} + \nabla\cdot[\kappa\nabla(p-p_0)]\\
&\frac{\partial\boldsymbol{v}}{\partial t} = -\boldsymbol{v}\cdot\nabla\boldsymbol{v} + (\boldsymbol{J}\times\boldsymbol{B}-\nabla p)/\rho + \nabla\cdot[\nu\nabla(\boldsymbol{v}-\boldsymbol{v}_0)]\\
&\frac{\partial\boldsymbol{B}}{\partial t} = -\nabla\times\boldsymbol{E}
\end{aligned} \tag{5}$$

with

$$\boldsymbol{J} = \nabla\times\boldsymbol{B}, \quad \boldsymbol{E} = -\boldsymbol{v}\times\boldsymbol{B} + \eta(\boldsymbol{J}-\boldsymbol{J}_0-\delta\boldsymbol{J}_{\text{bs}}) \tag{6}$$

where ρ, p, v, $\boldsymbol{B}$, $\boldsymbol{E}$, and $\boldsymbol{J}$ denote the plasma density, thermal pressure, plasma velocity, magnetic field, electric field, and current density, respectively. The subscript "0" denotes the equilibrium state. The perturbation of the bootstrap current $\delta\boldsymbol{J}_{\text{bs}} = \boldsymbol{J}_{\text{bs}} - \boldsymbol{J}_{0,\text{bs}}$ has been included in Ohm's law. Both the bootstrap current $\boldsymbol{J}_{\text{bs}}$ and the equilibrium bootstrap current $\boldsymbol{J}_{0,\text{bs}}$ are computed in the kinetic model. The term $\eta\boldsymbol{J}_0$

indicates Ohmic heating to sustain the plasma current. Γ (= 5/3) represents the ratio of specific heat of plasma. η, D, κ, and v represent the resistivity, the plasma diffusion coefficient, the thermal conductivity, and the viscosity, respectively. The parameters are chosen to be $\eta = 1.0\times10^{-5}$, $D = 1.0\times10^{-5}$, $\kappa_{\perp} = 1.0\times10^{-6}$, $\kappa_{||} = 5.0\times10^{-2}$, and $v = 1.0\times10^{-5}$. The variables are normalized as follows: $\boldsymbol{B}/B_{00}\rightarrow\boldsymbol{B}$, $\boldsymbol{x}/a\rightarrow\boldsymbol{x}$, $\rho/\rho_{00}\rightarrow\rho$, $\boldsymbol{v}/v_{\mathrm{A}}\rightarrow\boldsymbol{v}$, $t/\tau_{\mathrm{A}}\rightarrow t$, $p/(B_{00}^2/\mu_0)\rightarrow p$, $J/(B_{00}/\mu_0 a)\rightarrow J$, $\boldsymbol{E}/(v_{\mathrm{A}}B_{00})\rightarrow\boldsymbol{E}$ and $\eta/(\mu_0 a/\tau_{\mathrm{A}})\rightarrow\eta$, where a is the minor radius, B_{00} and ρ_{00} are the initial magnetic field and the plasma density at the magnetic axis, respectively. $v_A = B_{00}/\sqrt{\mu_0\rho_{00}}$ and $\tau_{\mathrm{A}} = a/v_{\mathrm{A}}$ are the Alfvén speed and Alfvén time at the magnetic axis. In the bootstrap current module, the effective collision frequency ($\nu^* = \nu_{\mathrm{c}}/\nu_{\mathrm{bounce}} = \varepsilon^{-3/2}\nu_{\mathrm{c}}qR_0/v_{\mathrm{th}}$) is defined as the physical collision frequency (ν_{c}) normalized by the bounce frequency ($\nu_{\mathrm{bounce}} = \varepsilon^{3/2}v_{\mathrm{th}}/qR_0$), where $\varepsilon = r/R_0$ is the inverse aspect ratio, v_{th} is the electron thermal velocity. The relation between the Alfvén time and the collision time τ_{c} can be expressed as $\tau_{\mathrm{c}} = \left[\varepsilon^{-3/2}qR_0/av^*k\right](\tau_{\mathrm{A}})$.

The flow chart of kinetic NTM is shown in figure 1. We will use a high accuracy nonlinear MHD code, in combination with a new developed kinetic bootstrap current model to study crucial NTM dynamics associated with the bootstrap current.

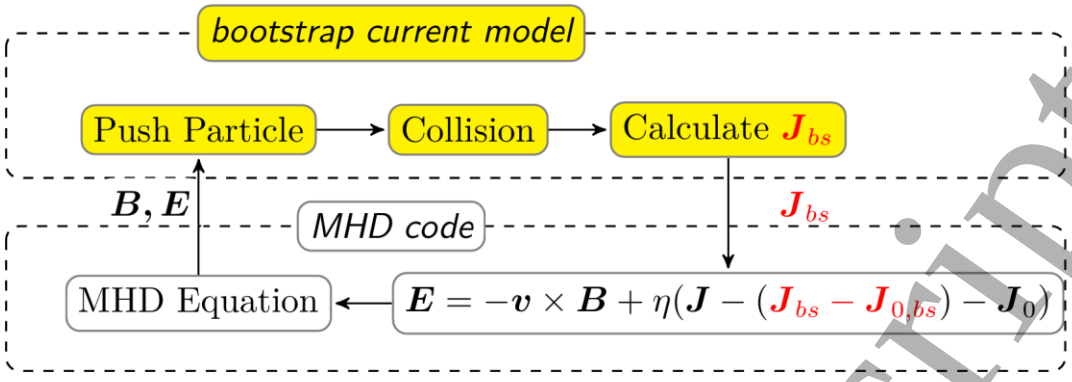

Figure 1. Flow chart of kinetic NTM includes the bootstrap current (yellow) and MHD modules (white). In the bootstrap current module, the δ*f* method of the kinetic equation (equation (2)) is adopted with particle-in-cell (PIC). The Monte Carlo pitch angle scattering model (equation (3)) is implemented to update the electron pitch angle in collisional process. The bootstrap current J_{bs} computed in the kinetic model is imported into the Ohm's law (equation (6)) of the MHD model. The fields are updated by a set of resistive MHD equations (equations (5) and (6)) and the magnetic and electric fields are feedback to the bootstrap current module.

2.2. Verification of bootstrap current calculation

To benchmark our results against analytic predictions in the absence of magnetic islands, we adopt plasma parameters with a major radius $R_0 = 3$ m, a minor radius $a = 1$ m, and the magnetic field at the magnetic axis $B_0 = 1$ T. A uniform mesh of size 128×16×128 (R, ϕ, Z) is utilized for both MHD and kinetic simulations, with a resolution of $\Delta R = 0.015$ m, $\Delta\phi = \pi/8$, and $\Delta Z = 0.015$ m. The kinetic model employs a total of 6×10^5 particles. Employing a combination of OpenACC and MPI technologies, MHD simulations are further parallelized using NVIDIA GPUs [37].

Figure 2(a) presents the safety factor q and the normalized density profiles n_e/n_{e0}, where n_{e0} represents the density at the magnetic axis, assuming a uniform temperature profile, thereby neglecting temperature gradients and simplifying equation (2) to $\kappa = \nabla n_0 / n_0$. Although this simplification overlooks the contribution of the temperature gradients to the bootstrap current, it facilitates the model validation. In reality, the temperature gradients alongside the density gradients contribute to the bootstrap current.

The impact of the temperature flattening within islands on the bootstrap current profile parallels that of the density flattening [26, 38].

The flux surface average of the bootstrap current $\langle J_{bs}\rangle$ within a selected magnetic surface is computed as $\langle J_{bs}\rangle = \langle J_{\parallel}\rangle - \langle J_{ps}\rangle$, where both J_{ps} and $J_{\parallel}$ are obtained from equation (4). J_{ps} and $J_{\parallel}$ are calculated in collisionless and collisional processes, respectively, shown in figure 3. The magnetic surface selected corresponds to the safety factor q = 2, with r = 0.45 and ε = 0.15, and a range of cases for different effective collision frequencies ν^* are examined. The flux surface-averaged bootstrap current $\langle J_{bs}\rangle$ attains a steady state. Consequently, $\langle J_{bs}\rangle$ is normalized by the collisionless limit value, $\langle J_{bs}\rangle$, calculated at a low collisional frequency $\nu^*\sim10^{-3}$. In Hinton's analytical solution (1976) [21, 39], the normalized analytical bootstrap current, dependent on the effective collision frequency ν^*, is expressed as $1\Big/\left(1+\sqrt{\nu^*}+a\cdot\nu^*\right)$.

Another analytical formula, based on the Sauter model [40, 41] is $\langle j_{\parallel}B\rangle = -IpL_{31}\,\partial\ln n/\partial\psi$ (equation (2) from reference [41]). Here, we solely consider the contribution of the electron density gradient. The trapped fraction at q = 2 is $f_{trap} = 1-3/4\langle B^2\rangle\int_0^{1/B_{max}}\lambda\mathrm{d}\lambda\Big/\langle\sqrt{1-\lambda B}\rangle = 0.53$. The coefficient L_{31} can be expressed as equation (10) for the Sauter-Redl model [41] or equation (A8) for the Sauter-Hager model [42]. The bootstrap current is normalized by the collisionless limit value. Figure 4(a) illustrates the scaling of the bootstrap current with the analytical formula of the Sauter-Redl model. Simulation results align closely with analytic theories, demonstrating the accuracy of our numerical scheme in calculating the bootstrap current. Figure 4(b) depicts the bootstrap current reaching a steady state within several collision times. The timescale for the magnetic field diffusion is $\tau_\eta = L^2/\eta$, where L denotes the typical length scale. It is imperative to ensure that the magnetic topology changes gradually to allow the bootstrap current to reach a steady state, implying that the magnetic field diffusion time (τ_η) must exceed the collision time (τ_c). In

subsequent simulations, the estimated magnetic field diffusion time and collision time are $1000\tau_A$ and $300\tau_A$, respectively.

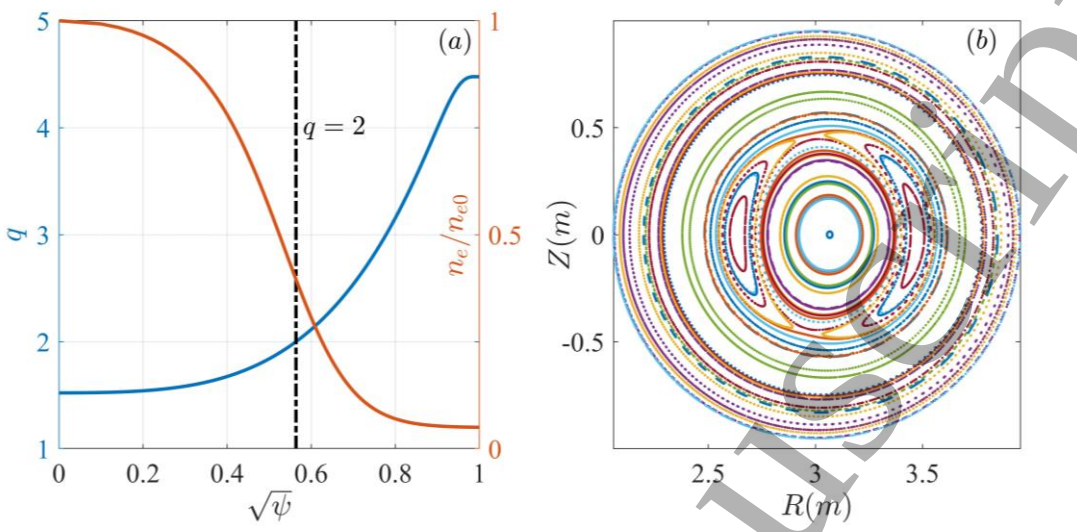

Figure 2. (a) Profiles of the initial safety factor and the normalized density, (b) Poincaré plots of the (2, 1) magnetic islands on the poloidal cross-section of the toroidal angle $\phi = 0^o$.

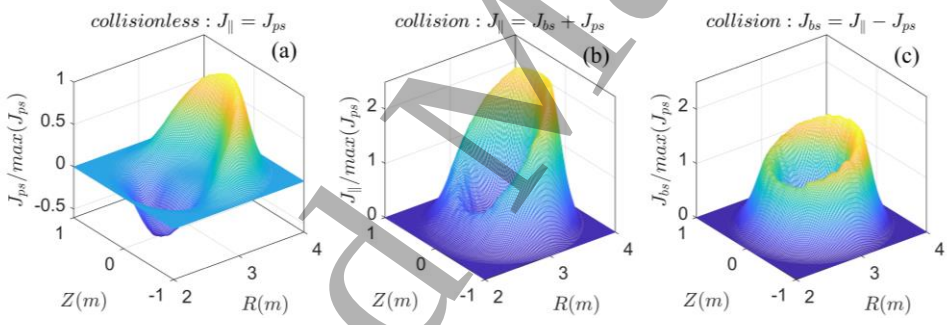

Figure 3. (a) The Pfirsch-Schlüter current (J_{ps}) is calculated without collisional process, (b) the parallel current ($J_{\parallel}$) in collision process, and (c) the bootstrap current J_{bs}.

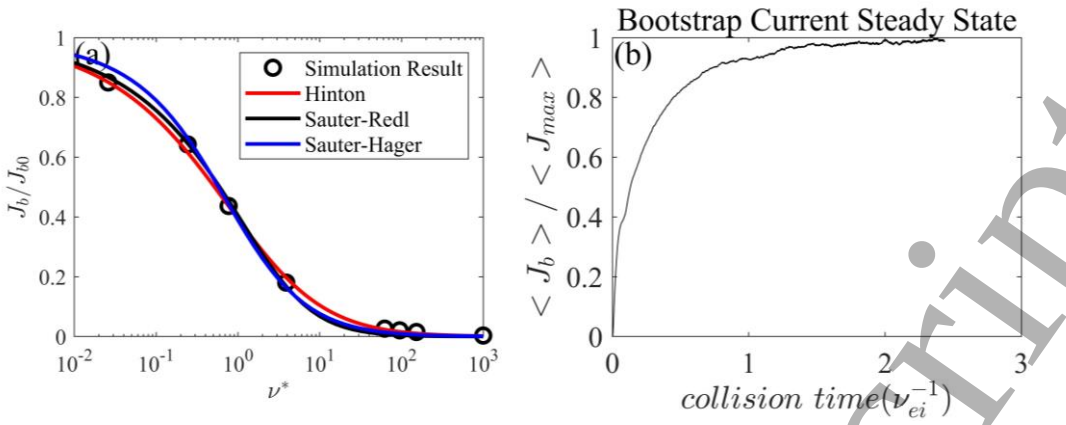

Figure 4. (a) Scaling of the bootstrap current $<J_{bs}>$ (normalized by $<J_{bs}>$ with a low collisional frequency $\nu^*\sim10^{-3}$) as a function of the effective collisional frequency ν^* at the q = 2 surface. The simulation result is benchmarked with the analytical formulae of the Hinton, Sauter-Redl, and Sauter-Hager models. (b) The time evolution of the bootstrap current that reaches an asymptotic value in several collision times.

3. Simulation results

3.1. Electron density flattening by magnetic island

In the subsequent section, we maintain the same initial equilibrium and parameters as in the previous section, depicted in figure 2(a). The instability parameter Δ' for the m/n = 2/1 TM exceeds 1, indicating that the m/n = 2/1 TM is unstable [43]. The m/n = 2/1 islands are computed using the CLT code, as illustrated in figure 2(b). The electron density in the kinetic model is described by $n_e = \int f \mathrm{d}v^3 = \sum_{i=1}^{N} f_0^i/(1-w_i)\delta(\boldsymbol{X}-\boldsymbol{X}_i)$. Figures 5 and 7 present surface plots of the electron density on the poloidal cross-sections at toroidal angles ϕ = 0° and ϕ = 180°, respectively. The formation of magnetic islands leads to flattened electron density due to a rapid parallel particle transport along magnetic field lines, illustrated by black dot and solid lines. The response of trapped and passing electrons to the magnetic island differs significantly. Passing electrons move rapidly along field lines, resulting in a uniform density distribution on each flux surface within magnetic islands. Conversely, trapped electrons exhibit a non-uniform density distribution due to their movement across different flux surfaces, influenced by

the mirror effect. Consequently, the electron density profile is less flattened on the Low Field Side (LFS) compared to the High Field Side (HFS), as evident in figure 5(c) and (d). To highlight the discrepancy between HFS and LFS, figure 6 portrays the same Y-scale in both figures 5(c) and (d) with the effective collisional frequency ν^*.

In regions of low collisionality ($\nu^* < 1$), electron collisions contribute to a more flattened electron density profile inside the islands at $\phi = 0^o$ on the LFS, illustrated by the blue solid line ($\nu^* = 0.1$) in figure 5(d) and 6(b). Similar phenomena occur at the poloidal cross-section with the toroidal angle $\phi = 180^o$, where the O-points of the islands lie at the $R = R_{\text{axis}}$ plane, as depicted by the blue solid line ($\nu^* = 0.1$) in figure 7(d). Electron collisions mitigate the discontinuity in velocity distribution at the trapped–passing boundary. The influence of scattering from trapped to passing further flattens the electron density profile. However, in fully collisional plasmas ($\nu^* > 1$), strong radial transport diminishes the flattening of electron density profiles. As shown in figures 5, 7(c) and (d), with a green solid line ($\nu^* = 5$), higher effective collisional frequencies result in weaker electron density profile fattening.

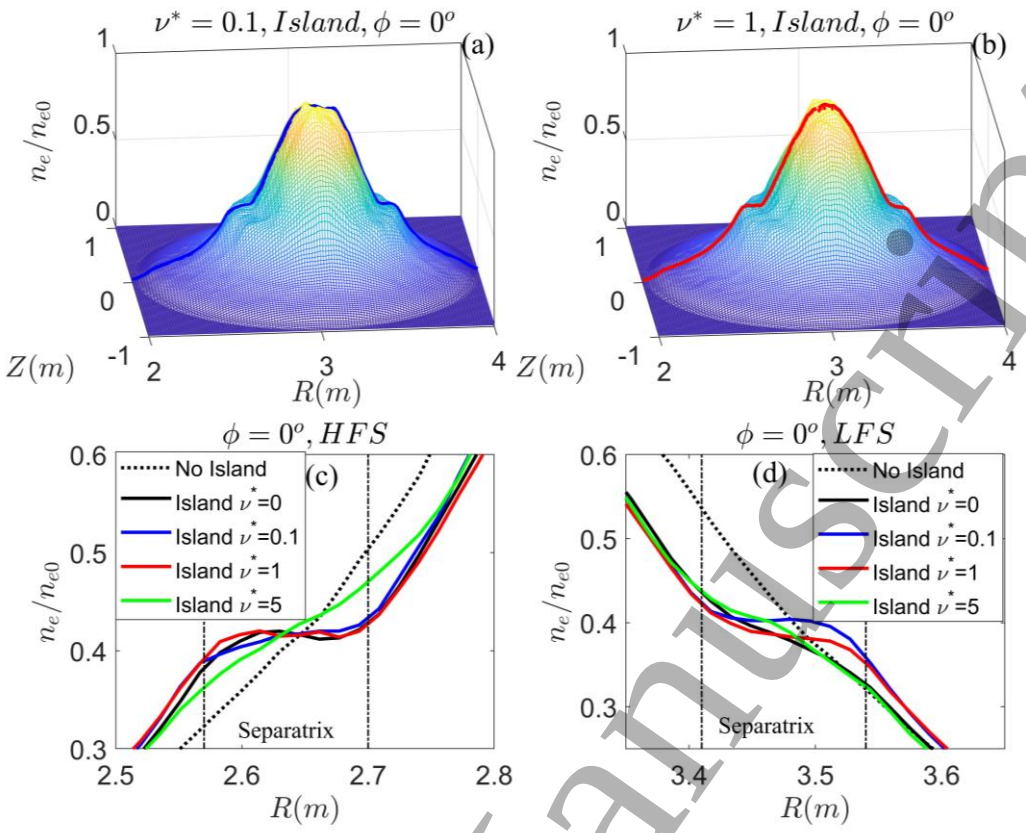

Figure 5. Kinetic simulation shows the surface plots of the electron density at the poloidal cross-section of the toroidal angle ϕ = 0º for a static magnetic island with (a) ν^* = 0.1 and (b) ν^* = 1. To exhibit the effect of ν^* on the electron density distribution, we draw the electron density profile at the middle plane Z = 0 together in (c) HFS and (d) LFS. The separatrix of the magnetic islands is also presented by the vertical black line in (c) and (d).

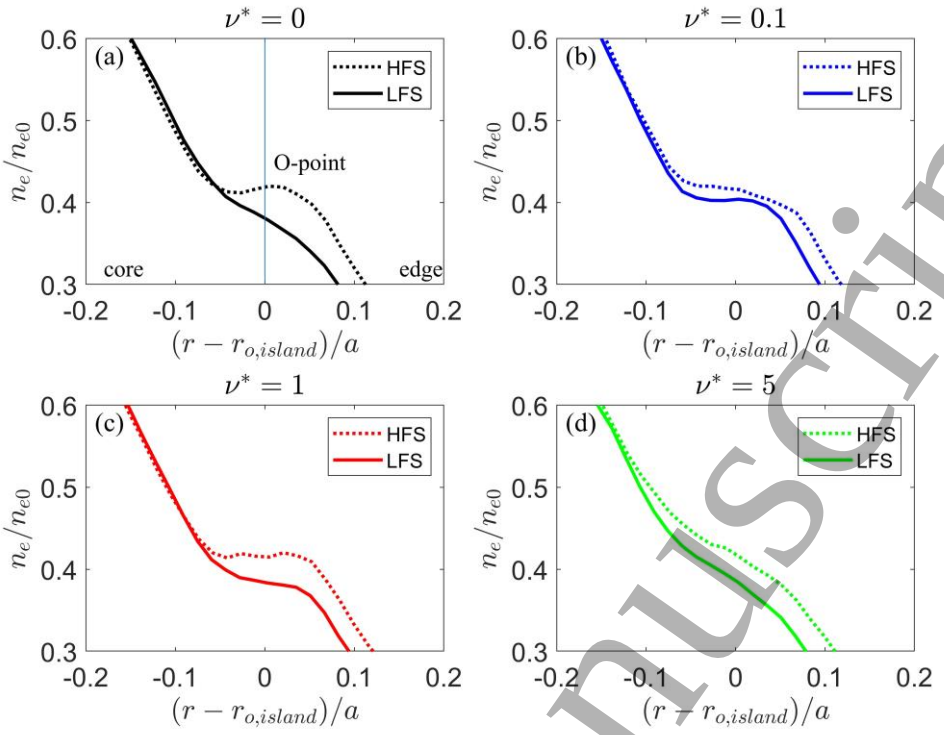

Figure 6. Kinetic simulation shows electron density on the HFS (dotted line) and LFS (solid line) with the effective collisional frequency ν^*, (a) $\nu^* = 0$, (b) $\nu^* = 0.1$, (c) $\nu^* = 1$ and (d) $\nu^* = 5$. $r_{o,island}$ presents the position of the O-point of magnetic island.

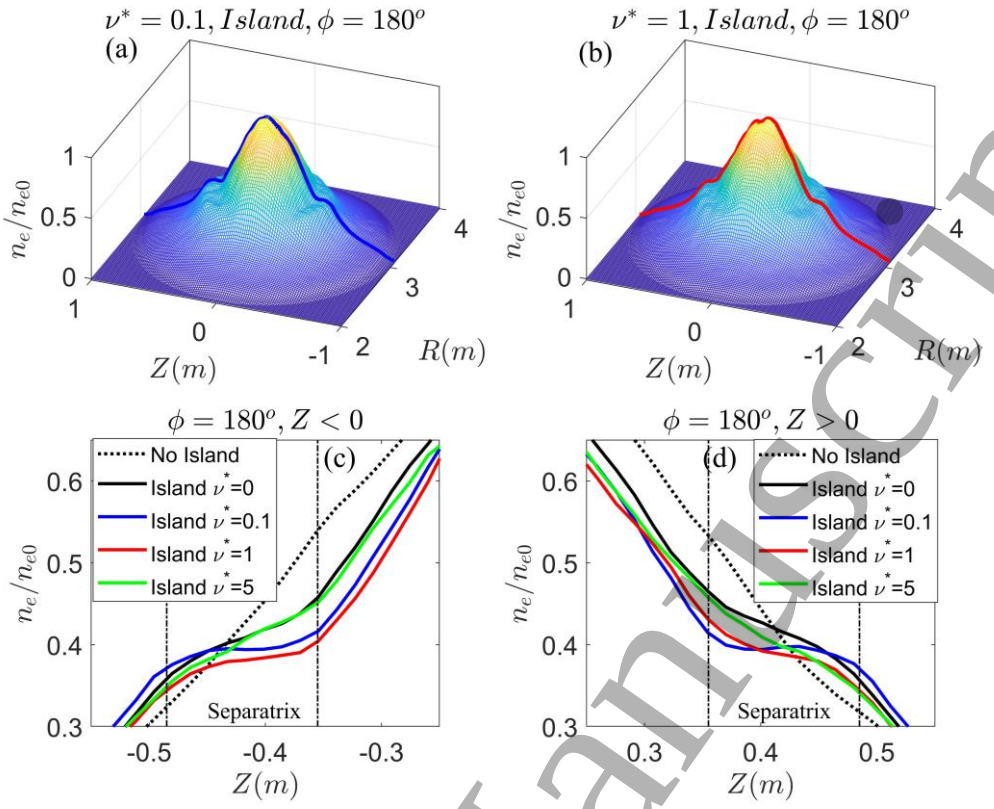

Figures 7. The rotation of the 2/1 magnetic islands for the toroidal angle $\phi = 180^o$. Kinetic simulation shows surface plots of the electron density at the poloidal cross-section with a static magnetic island for (a) $v^* = 0.1$ and (b) $v^* = 1$. To show the effect of v^* on the density distribution, we draw the electron density profile at the $R = R_0$ plane together in $Z < 0$ (c) and $Z > 0$ (d). The separatrix of the magnetic islands is also presented by the vertical black line in (c) and (d).

3.2. Bootstrap currents in static and dynamic magnetic islands

We maintain the same initial equilibrium and parameters as in the previous section. Utilizing an initial equilibrium with $q = 2$, we calculate the tearing mode instability with $m/n = 2/1$ islands in the MHD model. The magnetic island is selected upon saturation of the tearing mode. The field comprises both perturbed magnetic ($\delta\boldsymbol{B}$) and electric ($\delta\boldsymbol{E}$) fields associated with magnetic islands due to magnetic reconnection. When only the perturbed magnetic field $\delta\boldsymbol{B}$ is retained and the perturbed electric field $\delta\boldsymbol{E}$ is removed in the kinetic model, we refer to the magnetic island as a "static magnetic island". When both the perturbed electric and magnetic field ($\delta\boldsymbol{E}$ and $\delta\boldsymbol{B}$) are self-consistently

included in the kinetic model, it constitutes a "dynamic magnetic island". The associated bootstrap current is termed "dynamic bootstrap current". We investigate the bootstrap current within "static magnetic islands" and "dynamic magnetic islands", separately.

The bootstrap currents inside the static islands with different values of the ratio w_b/W in the banana regime have been investigated in reference [18]. Dong *et al* have studied the effect of the collisional frequency v^* on the bootstrap currents inside the static magnetic islands in detail [26]. In order to focus the effects of dynamic magnetic islands on the bootstrap currents, the results of the bootstrap current with effective collisional frequency $v^* = 0.1$ (the banana regime) are presented only.

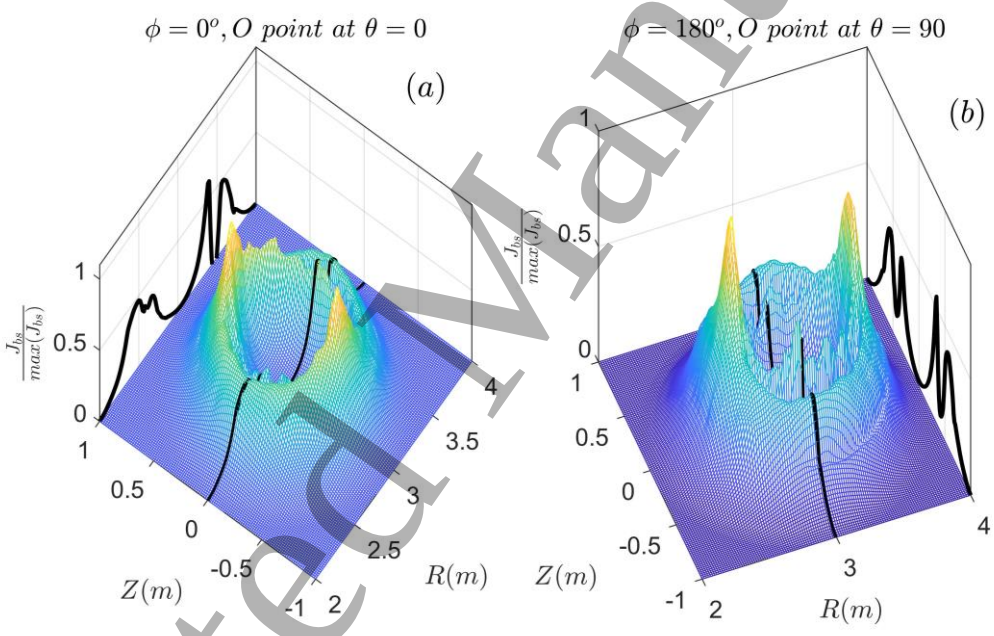

Figure 8. (a) The bootstrap current density at the poloidal cross-section of the toroidal angle $\phi = 0^o$ together with 2-D plot for $\boldsymbol{J}_{bs}/\max(J_{bs})$ versus R at $Z = 0$ (black solid line); (b) the bootstrap current density at the poloidal cross-section of the toroidal angle $\phi = 180^o$ together with 2-D plot for $\boldsymbol{J}_{bs}/\max(J_{bs})$ versus Z at $R = R_0$ (black solid line).

Conventional understanding suggests that a static magnetic island reduces the plasma pressure gradient through parallel particle transport, consequently diminishing the bootstrap current inside islands, as depicted in figures 8(a) and (b). However, a dynamic magnetic island induces a perturbed electric field ($\delta\boldsymbol{E}$) during the development

of the tearing mode instability, as shown in figures 9(a) and (b). Some charged particles experience energy gain or loss due to acceleration or deceleration by the parallel electric field $\boldsymbol{E}_{//}=(\boldsymbol{E}\cdot\boldsymbol{b})\boldsymbol{b}$ in figure 9(c). The radial electric field $\boldsymbol{E}_r$ can influence the drift displacement and trajectory of charged particles. Therefore, the perturbed electric field (where $\boldsymbol{E}=\delta\boldsymbol{E}$) induced by a dynamic magnetic island enables certain charged particles to cross the trapped-passing boundary and alter their orbits, significantly modifying the bootstrap current.

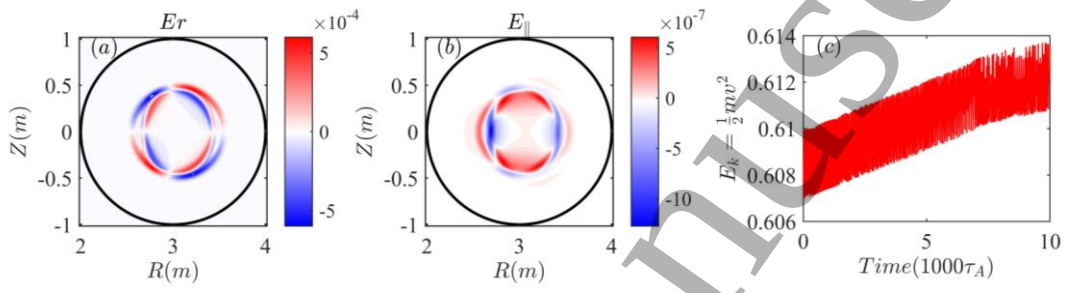

Figure 9. Contour plots of (a) the radial electric field $\boldsymbol{E}_r$ and (b) the parallel electric field $\boldsymbol{E}_{//}$ on the poloidal cross-section of the toroidal angle $\phi = 0^{\circ}$ for the $m/n = 2/1$ tearing mode, which is corresponding to figure 11 at time = $21000\tau_A$. (c) Charged particles gain or loss energy because of accelerating or decelerating by the parallel electric field.

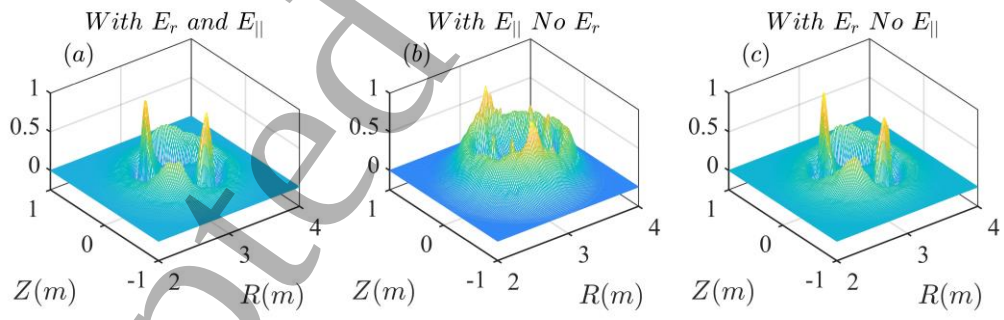

Figure 10. Surface plots of the dynamic bootstrap current at time = $250\tau_A$ after (a) imposing the perturbed $\boldsymbol{E}$ (= $\boldsymbol{E}_r$ + $\boldsymbol{E}_{//}$), (b) imposing the perturbed $\boldsymbol{E}_{//}$ and removing of $\boldsymbol{E}_r$, and (c) imposing the perturbed $\boldsymbol{E}_r$ and removing of $\boldsymbol{E}_{//}$.

Comparing with figure 8 in static magnetic islands where $\boldsymbol{E}$ = 0, we observe the bootstrap current affected by the perturbed electric field $\boldsymbol{E}$ in figure 10. Additionally, three additional modeling cases are presented in figure 10. In case (a), the bootstrap current is calculated with the retention of both the perturbed parallel and radial electric

fields ($\boldsymbol{E}_{//}$, $\boldsymbol{E}_r$) in figure 10(a). In case (b), $\boldsymbol{E}_{//}$ is retained, but $\boldsymbol{E}_r$ is removed in figure 10 (b). In case (c), $\boldsymbol{E}_r$ is retained, but $\boldsymbol{E}_{//}$ is removed in figure 10(c). By comparing the bootstrap current density in cases (a), (b), and (c) in figure 10, we find that the bootstrap current density in case (a) is similar to that in case (c), rather than in case (b). The bootstrap current density is predominantly influenced by the radial electric field $\boldsymbol{E}_r$ rather than the parallel electric field $\boldsymbol{E}_{//}$ since $\boldsymbol{E}_r$ is much larger than $\boldsymbol{E}_{//}$ in the tearing mode instability as shown in figure 9(a) and (b). The radial electric field $\boldsymbol{E}_r$ could cause the $\boldsymbol{E}\times\boldsymbol{B}$ drift, which can noticeably modify the bootstrap current. This causes the rotation of the magnetic island, which will be discussed in section 3.3.

3.3. Dynamic responses of magnetic islands to bootstrap currents

The perturbation of the bootstrap current due to the pressure flattening inside magnetic islands can significantly impact the growth of a tearing mode. In the general scenario of a classical tearing mode, the island dynamics, driven solely by magnetic free energy until the island saturates, are depicted by the solid black line in figure 11. Subsequently, the bootstrap current density is computed in "static" or "dynamic" magnetic islands when the tearing mode reaches saturation at time = $21000\tau_A$. At this point, the bootstrap current constitutes nearly 10.0 percent of the total plasma current at the $q = 2$ surface. The bootstrap current activates at time = $21000\tau_A$, as illustrated in the flow chart in figure 1. In subsequent simulations, the bootstrap current $\boldsymbol{J}_{bs}$ is calculated in the kinetic model and imported in Ohm's law of the MHD model. Then, the fields, including the magnetic ($\boldsymbol{B}$) and electric ($\boldsymbol{E}$) fields, are updated using a set of resistive MHD equations (equations (5) and (6)). The updated $\boldsymbol{B}$ and $\boldsymbol{E}$ are imported from the MHD to push electrons in the kinetic model. Note that in the case of static magnetic islands, the electric field $\boldsymbol{E}$ is not set to 0 in the MHD model. However, $\boldsymbol{E}$ is artificially set to 0 to calculate the bootstrap current in the kinetic model. Therefore, the bootstrap currents are updated during subsequent reconnection. The dynamic responses of "static" or "dynamic" magnetic islands to bootstrap currents are investigated

respectively in the following.

Figure 11 illustrates the time evolution of the m/n = 2/1 magnetic island driven by static (blue line) and dynamic (red line) bootstrap currents. The width of magnetic islands increases rapidly and saturates again for both cases. The saturated island width is 0.133a without the bootstrap current, 0.161a with the static bootstrap current, and 0.15a with the dynamic bootstrap current. The island width with the static or dynamic bootstrap current increases by 21% and 14%, respectively. According to the analytical theory, the perturbation of the bootstrap currents plays a destabilizing role in the nonlinear island.

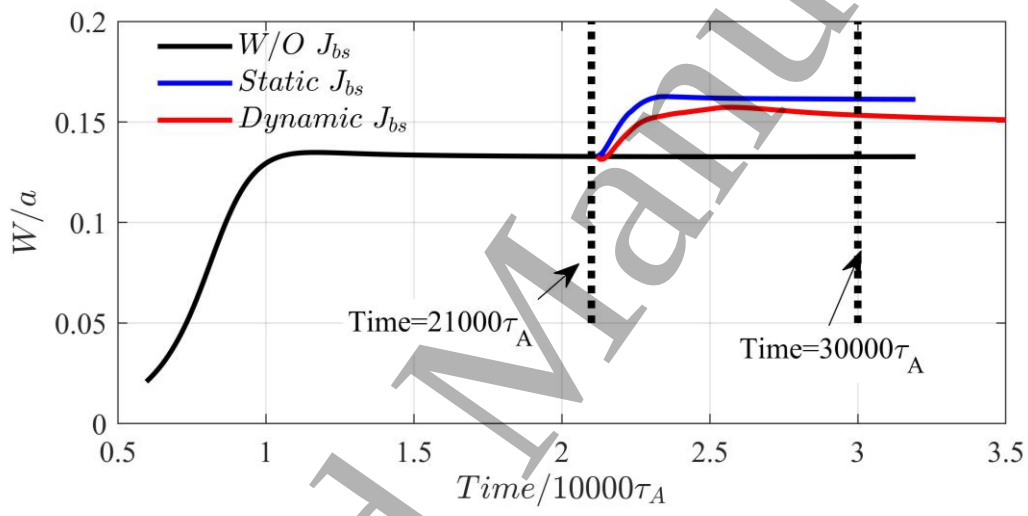

Figure 11. Time evolutions of the width of the m/n = 2/1 magnetic island driven without the bootstrap current (black line)/with the bootstrap current for the static island (blue line)/ in the dynamic island (red line).

We also observe that the saturated island width in the dynamic case is smaller than that in the static case. Additionally, magnetic islands do not rotate in the static case but rotate in the dynamic case, as shown in figure 12. The primary reason for this phenomenon is that the radial reconnection electric field $\boldsymbol{E}_r$ associated with the dynamic island leads to an asymmetric distribution of the bootstrap current in the vicinity of the X-point in the kinetic part. Consequently, this asymmetric bootstrap current will cause the rotation of the island in the MHD part. The island rotation plays a stabilizing effect in the development of the tearing mode.

Specifically, during the reconnection process, the reconnection electric field modifies the orbits of electrons, resulting in a net drift of electrons. In the rest frame of the islands, electrons drift inside the islands under the $\boldsymbol{E}\times\boldsymbol{B}$ influence, subsequently modifying the bootstrap current, as shown in figure 13(b). Moreover, the asymmetrically distributed bootstrap current in the surrounding area of the X-point leads to the loss or gain of magnetic flux. Consequently, the saturated magnetic island rotates due to an asymmetric perturbation bootstrap current in the dynamic island, as depicted in figures 12 and 13(b). Any rotation of magnetic islands, which could also result from plasma toroidal rotation or diamagnetic drift effect, plays a stabilizing role in the development of the tearing mode. Our preliminary results suggest that the retaining reconnection electric field resulting from dynamic islands leads to the rotation and the lower saturation level of magnetic islands.

In the present work, the radial reconnection electric field $\boldsymbol{E}_r$ associated with the dynamic island induces island rotation, i.e., the island rotation is not associated with the diamagnetic effect. It is also evident that the island does not rotate in the case with the static island, considering only the electron population and ignoring the ion contribution to the bootstrap current. The initial (seed) island (at time = $21000\tau_A$) does not rotate because the plasma flow is zero. The time variation of the electric field $\boldsymbol{E}$ associated with the dynamic island is very slow ($\mathrm{d}\boldsymbol{E}/\mathrm{d}t \approx 0$). Therefore, drift displacements of species caused by the polarization drift $\mathrm{d}\boldsymbol{E}/\mathrm{d}t$, instead of the $\boldsymbol{E}\times\boldsymbol{B}$ drift, may not be significant. In this case, the initial magnetic island width is rather large ($W = 0.133a$), so the polarization effect ($\sim(\rho_{\mathrm{bi}}/W)^2$, ρ_{bi} is the ion banana width) is not significant [44]. Nevertheless, the polarization effect associated with the dynamic island and the plasma rotation may be important, which will be investigated in future work.

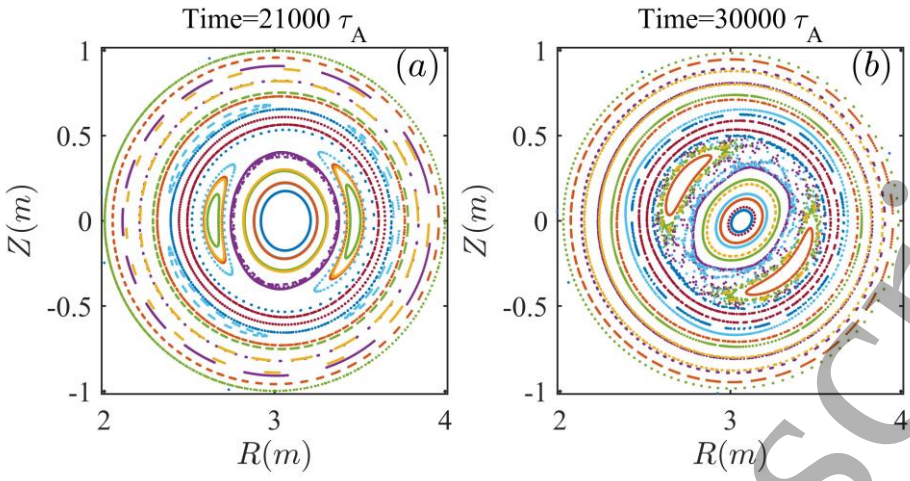

Figure 12. Snapshots of the topology of magnetic islands for the dynamic case in the toroidal cross sections ϕ = 0°, (a) time at 21000τ_A and (b) time at 30000τ_A.

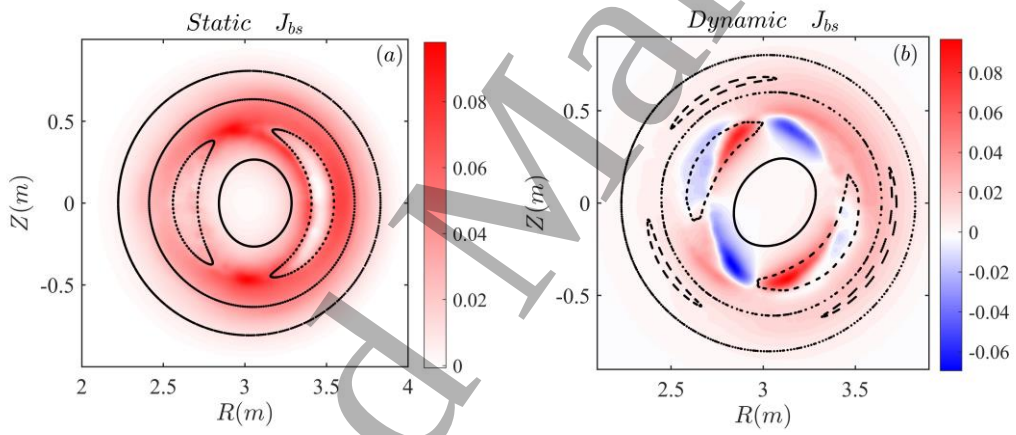

Figure 13. Contour plot of the bootstrap current (normalized by <J_0> at the q = 2 surface) in the static (a) and dynamic (b) magnetic island and Poincaré plots of magnetic islands (dotted line) for the toroidal cross section ϕ = 0° at time = 30000τ_A.

We address the issue of the nonlinear NTM threshold for the m/n = 2/1 mode, comparing the Rutherford prediction and our kinetic-NTM simulation results. The evolution of the magnetic island width W with NTM can be expressed by the modified Rutherford's equation as follows [45, 46]:

$$0.823\frac{\mathrm{d}W}{\mathrm{d}t}=\frac{\eta}{\mu_0}\left(\Delta'+6.34\frac{j_{\mathrm{bs}}}{B_{\mathrm{ps}}\left(1/L_{q_0 s}+j_{\mathrm{bs}}/B_{\mathrm{ps}}\right)W}\right) \tag{7}$$

where η is the resistivity. $L_{q_0 s}=q_0/q_0'\left(r=r_s\right)$, q_0 and B_{ps} are the safety factor and the equilibrium poloidal magnetic field at the rational surface $r = r_s$. The parameter Δ' can be represented in the form of W in equation (12) in reference [47].

$$\Delta'=0.41W\left\{a_*^2\left[\ln\left(\frac{1}{W}\right)+4.85-\frac{0.68}{2-s}\right]-\frac{Aa_*}{2}-b_*\right\}-0.18\left(a_*/r_s\right)W \tag{8}$$

where $a_*=\left(1-2/s\right)L\,J_{\mathrm{eq}}'/J_{\mathrm{eq}}$ and $b_*=\left(1-2/s\right)L^2\,J_{\mathrm{eq}}''/J_{\mathrm{eq}}$ are evaluated at the rational surface. s and J_{eq} are the magnetic shear and the equilibrium current density. L is a convenient normalization scale. In our calculation, we choose a proper parameter A to ensure that the classical tearing mode is unstable at $\Delta'\left(W=0\right)>0$, and the magnetic island saturates at $W = 0.133a$ for the classical tearing mode (black line), as shown in figure 14. Then the bootstrap current J_{bs} is imported at time = $15000\tau_{\mathrm{A}}$ when the tearing mode saturates. It is found that the bootstrap current is nearly 10.0 percent of the total plasma current at the $q = 2$ surface, which is the same as we do in our kinetic-NTM simulation. The width of the magnetic island ascends rapidly and saturates again. The saturated width of the magnetic island is $W = 0.168a$ (blue line). Furthermore, we also carry out the cases with the bootstrap current imported at $W = 0.01a$ (blue dashed line) and at $W = 0.1a$ (red dashed line). The saturated width of the magnetic island is also $W = 0.168a$. Compared with the results shown in figures 11 and 14, we observe good agreement.

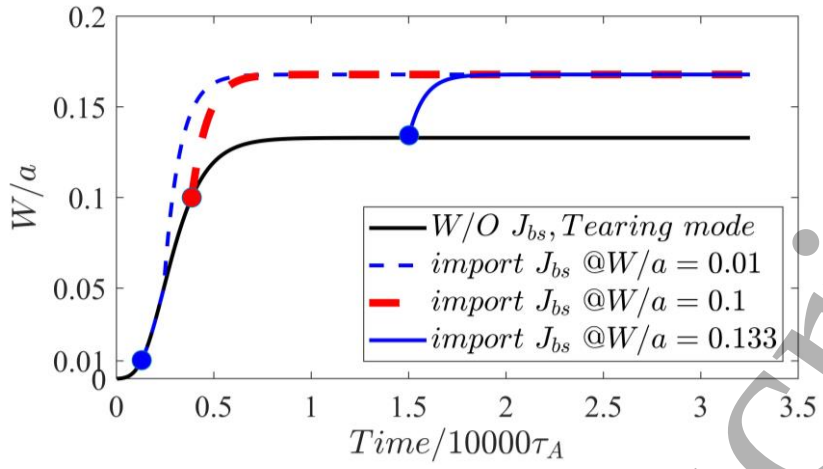

Figure 14. The time evolutions of the width of the m/n = 2/1 magnetic island calculated from the Rutherford equation. The blue dashed, red dashed, blue lines are for the cases that the bootstrap currents were imported when $W = 0.01a$, $0.1a$, $0.133a$, respectively. The black line is for the case without the bootstrap current. The bootstrap current is nearly 10.0 percent of the total plasma current at the $q = 2$ surface, and the saturated width of the magnetic island is $W = 0.168a$.

4. Conclusion

In conclusion, our study investigates the interaction of the dynamic magnetic island with the bootstrap current using magnetohydrodynamic (MHD)-kinetic-hybrid simulation. We employed the initial equilibrium with $q = 2$ to examine the tearing mode instability with the m/n = 2/1 island, which is particularly significant in tokamak experiments. Instead of imposing the static and artificial magnetic island perturbations, we calculated the perturbed magnetic and electric fields associated with the dynamic magnetic islands from a MHD code (CLT). It is well known that both perturbed magnetic and electric fields are generated during magnetic reconnection or tearing mode development. If the perturbed electric field $\boldsymbol{E}$ is removed and only the perturbed magnetic field $\boldsymbol{B}$ retains, we call it as a "static magnetic island". If both the perturbed magnetic and electric fields $\boldsymbol{B}$ and $\boldsymbol{E}$ are retained, we call it as a "dynamic magnetic island".

Here are the main findings of our study:

(1) Plasma density distribution:

Inside magnetic islands, electron density is flattened due to fast parallel transport of electrons along magnetic field lines. Trapped electrons predominantly reside in the LFS, resulting in a less flattened electron density profile in LFS compared to HFS. Moreover, in regions of low collisionality ($\nu^* < 1$), electron collisions contribute to further flattening of electron density profiles inside the islands. The effectiveness of this flattening diminishes with increasing collision frequency (ν^*) due to enhanced radial transport.

(2) Effects of static and dynamic magnetic islands on bootstrap current:

The bootstrap current is reduced as expected in islands. But in the dynamic magnetic island, the induced electric field significantly alters the bootstrap current distribution.

(3) Dynamic responses and island rotation:

In both static and dynamic cases, the width of the magnetic island increases rapidly and saturates after the onset of the bootstrap current. In the dynamic case, the induced electric field significantly changes the bootstrap current distribution. The bootstrap current is mainly affected by the radial electric field $\boldsymbol{E}_r$. The radial electric field $\boldsymbol{E}_r$ could cause the $\boldsymbol{E}\times\boldsymbol{B}$ drift. Consequently, particles accumulate near the X point of magnetic islands, which can noticeably modify the bootstrap current. If the bootstrap current turns on when the tearing mode saturates, the width of the magnetic island ascends rapidly and saturates again for both the static and dynamic cases. In the dynamic case, the distribution of the bootstrap current in the vicinity of the X-points is strong asymmetric, which causes the rotation of the magnetic island. The island rotation leads to that the saturated level of the tearing mode is smaller in the dynamic case than in the static case.

In summary, our study provides insights into the complex interplay between magnetic islands and bootstrap currents in tokamak plasmas. The dynamic responses, particularly the induced rotation of magnetic islands and its impact on the tearing mode

saturation, are observed. The importance of considering dynamic effects in understanding tokamak plasma behavior is highlighted.

Acknowledgments

This work was supported by the National Key Research and Development Program of China (Nos. 2022YFE03100000, 2019YFE03020003 and 2019YFE03030004), and National Natural Science Foundation of China (Nos. 11835010, 12305236 and 12375224), and Innovation Program of Southwestern Institute of Physics (202301XWCX001).

Appendix A

In the guiding-center phase space ($\boldsymbol{X}$, $v_{//}$, μ, ζ), $\boldsymbol{X}$ and $v_{//} = \boldsymbol{b}\cdot\dot{\boldsymbol{X}}$ denote the guiding-center position and the guiding-center parallel velocity, respectively. μ is the magnetic moment and ζ is the gyrophase, which gives the location of the particle on the circle about the guiding center. The guiding-center phase-space Lagrangian is [34]

$$L_{\mathrm{gc}} = \left[\frac{e}{c}\boldsymbol{A} + mv_{//}\boldsymbol{b}\right]\cdot\dot{\boldsymbol{X}} + J\dot{\zeta} - H_{\mathrm{gc}} \tag{A.1}$$

where $J \equiv (mc/e)\mu$ is the gyroaction variable. The guiding-center Hamiltonian is given by

$$H_{\mathrm{gc}} = \frac{m}{2}v_{//}^2 + \mu B - e\Phi - \frac{m}{2}\left|\boldsymbol{v}_E\right|^2 \tag{A.2}$$

The magnetic field strength B and the electric and magnetic potentials (Φ, $\boldsymbol{A}$) are evaluated at the guiding-center position $\boldsymbol{X}$, not at the particle position. With manipulations similar to those used to derive the Lorentz force $\boldsymbol{F} = m\dfrac{\mathrm{d}\boldsymbol{v}}{\mathrm{d}t} = e\left(\boldsymbol{E} + \dfrac{1}{c}\boldsymbol{v}\times\boldsymbol{B}\right)$, we obtain the Euler-Lagrange equation.

$$m\frac{\mathrm{d}v_{//}}{\mathrm{d}t}\boldsymbol{b} = e\boldsymbol{E} - \mu\nabla B + \frac{m}{2}\nabla\left|\boldsymbol{v}_E\right|^2 - mv_{//}\frac{\partial \boldsymbol{b}}{\partial t} + \dot{\boldsymbol{X}}\times\left(\frac{e}{c}\boldsymbol{B} + mv_{//}\nabla\times\boldsymbol{b}\right)$$
$$\equiv e\left(\boldsymbol{E}^* + \frac{1}{c}\dot{\boldsymbol{X}}\times\boldsymbol{B}^*\right) \tag{A.3}$$

and the effective electromagnetic fields

$$e\boldsymbol{E}^* = e\boldsymbol{E} - \mu\nabla B + \frac{m}{2}\nabla\left|\boldsymbol{v}_E\right|^2 - mv_{//}\frac{\partial \boldsymbol{b}}{\partial t}$$
$$\frac{e}{c}\boldsymbol{B}^* = \frac{e}{c}\boldsymbol{B} + mv_{//}\nabla\times\boldsymbol{b} \tag{A.4}$$

the effective electromagnetic fields are defined as $\boldsymbol{B}^* = \nabla\times\boldsymbol{A}^*$ and $\boldsymbol{E}^* = -\nabla\Phi^* - \partial\boldsymbol{A}^*/\partial t$ .The effective electric and magnetic potentials

$$e\Phi^* = e\Phi + \mu B - \frac{m}{2}\left|\frac{\boldsymbol{E}\times\boldsymbol{B}}{B^2}\right|^2$$
$$\boldsymbol{A}^* = \boldsymbol{A} + \frac{mv_{//}}{Ze}\boldsymbol{b} \tag{A.5}$$

The electromagnetic field are $\boldsymbol{E} = -\nabla\Phi - \partial\boldsymbol{A}/\partial t$ and $\boldsymbol{B} = \nabla\times\boldsymbol{A}$. We obtain the rate of change of the variable $v_{//}$ by taking the scalar product of equation (A.3) with the effective magnetic field $\boldsymbol{B}^*$,

$$\frac{\mathrm{d}v_{//}}{\mathrm{d}t} = \frac{e}{m}\frac{\boldsymbol{B}^*}{B^*}\boldsymbol{E}^* \tag{A.6}$$

The vector product of equation (A.3) with $\boldsymbol{b}$, using $v_{//} = \boldsymbol{b}\cdot\dot{\boldsymbol{X}}$, yields the guiding-center velocity

$$\dot{\boldsymbol{X}} = \frac{1}{B_{//}^*}\left(v_{//}\boldsymbol{B}^* + c\boldsymbol{E}^*\times\boldsymbol{b}\right) \tag{A.7}$$

where $B_{//}^* = \boldsymbol{b}\cdot\boldsymbol{B}^*$ is the effective magnetic field $\boldsymbol{B}^*$ in the parallel direction.

Appendix B

In order to fully explain the Pfirsch-Schlüter current and calculate this current in our code, The linear MHD equations and the kinetic theory are revisited. In the axisymmetric equilibria, the magnetic field can be represented as $\boldsymbol{B} = \nabla\phi\times\nabla\psi + g\nabla\phi$,

where the ψ is the poloidal magnetic flux, g is a function of ψ, and ϕ is the toroidal angle. The parallel current can be calculated by combination of the force balance equation $\nabla P = \boldsymbol{J} \times \boldsymbol{B}$ in the perpendicular direction and the free divergence of the current density $\nabla \cdot \boldsymbol{J} = 0$:

$$\boldsymbol{J}_{\perp} = \frac{\boldsymbol{B} \times \nabla P}{B^2} \tag{B.1}$$

$$J_{\parallel} = -gP'/B - g'B \tag{B.2}$$

where the subscripts $\perp$ and $\parallel$ denote the perpendicular and parallel to the magnetic field, respectively. P represents the pressure, and the prime denotes the derivative with respect to ψ. equation (B.2) actually describes the so-called Pfirsch-Schlüter current. In order to introduce the method of how to calculate the Pfirsch-Schlüter current in the code, we describe the kinetic formalism. The Vlasov equation is

$$\frac{\mathrm{d}F}{\mathrm{d}t} = \left[\frac{\partial}{\partial t} + \boldsymbol{v} \cdot \nabla_x + \frac{q}{m} \left(\boldsymbol{E} + \boldsymbol{v} \times \boldsymbol{B} \right) \cdot \nabla_v \right] F = 0 \tag{B.3}$$

where F is the distribution function, q and m represent the species charge and mass, respectively. ∇_x and ∇_v denote the Laplace operators in the $\boldsymbol{x}$ and $\boldsymbol{v}$ space. We introduce the guiding center coordinates ($\boldsymbol{X}$, ε, μ, α), where $\boldsymbol{X}$ is the guiding-center position, ε is the particle energy, μ is the magnetic moment, and α is the gyrophase. In order to linearize the Vlasov equation (B.3) in the guiding center coordinates, F is decomposed to the equilibrium (F_{g}) and perturbed (δF_{g}) parts. Hence, the equilibrium Vlasov equation becomes [36],

$$\left(\dot{\boldsymbol{X}} \cdot \nabla_{\boldsymbol{X}} + \dot{\alpha} \frac{\partial}{\partial \alpha} \right) F_{\mathrm{g}} = 0 \tag{B.4}$$

where

$$\begin{aligned} \dot{\boldsymbol{X}} &= \boldsymbol{v}_{\parallel} \boldsymbol{e}_{\mathrm{b}} + \boldsymbol{v}_{\mathrm{d}} \\ \dot{\alpha} &= -\Omega\left(\boldsymbol{X} \right) + \dot{\alpha}_1 \end{aligned} \tag{B.5}$$

where $v_{\parallel}$ is the velocity of the guiding center in the direction of the magnetic field, $\boldsymbol{v}_{\mathrm{d}}$ is the drift velocity, including the magnetic curvature and gradient drift, $\Omega = ZeB/m$

is the gyrofrequency, the $\dot{\alpha}_1$ term is resulted from the guiding center transform of the gyrofrequency. The lowest order equilibrium Vlasov equation (B.4) becomes

$$\left(v_{\|}\boldsymbol{e}_{\mathrm{b}}\cdot\nabla-\Omega\frac{\partial}{\partial\alpha}\right)F_{\mathrm{g0}}=0 \tag{B.6}$$

The lowest order solution is the isotropic Maxwellian equilibrium distribution function $F_{g0}=n_0\left(\boldsymbol{X}\right)f_{\mathrm{M}}$. After taking gyrophase average, the next order kinetic equation is

$$v_{\|}\boldsymbol{e}_{\mathrm{b}}\cdot\nabla_{\boldsymbol{X}}F_{\mathrm{g1}}+\boldsymbol{v}_{\mathrm{d}}\cdot\nabla_{\boldsymbol{X}}F_{\mathrm{g0}}=0 \tag{B.7}$$

The solution is

$$F_{\mathrm{g1}}=-v_{\|}\frac{g}{\Omega}\frac{\partial F_{\mathrm{g0}}}{\partial\psi}+\mathrm{sign}\left(v_{\|}\right)F_{\mathrm{g1}}\left(\psi,\mu,\varepsilon\right) \tag{B.8}$$

where F_{g1} is the integration constant. We has

$$\begin{aligned}\boldsymbol{J}_{\perp}&=\sum_i q_i\int\boldsymbol{v}_{\perp}\left(F_{\mathrm{g0}}+F_{\mathrm{g1}}\right)\mathrm{d}^3v=\sum_i q_i\int\mathrm{d}^3v\boldsymbol{v}_{\perp}F_{\mathrm{g0}}\\&=\sum_i q_i\int\mathrm{d}^3v\boldsymbol{v}_{\perp}\frac{1}{\Omega}\times\boldsymbol{e}_{\mathrm{b}}\cdot\nabla F_{\mathrm{g0}}\\&=\frac{\boldsymbol{B}\times\nabla p}{B^2}\end{aligned} \tag{B.9}$$

Noting that F_{g1} does not contribute to the perpendicular current density due to being odd in $v_{\|}$. Therefore,

$$\begin{aligned}J_{\|}&=\sum_i q_i\int v_{\|}\left(F_{\mathrm{g0}}+F_{\mathrm{g1}}\right)\mathrm{d}^3v=\sum_i q_i\int\mathrm{d}^3vv_{\|}F_{\mathrm{g1}}\\&=-\frac{gp'}{B}-B\sum_i q_i\int\mathrm{d}\mu\mathrm{d}\varepsilon F_{\mathrm{g1}}\left(\psi,\mu,\varepsilon\right)\end{aligned} \tag{B.10}$$

It should also be noted that F_{g0} does not contribute to the parallel current density due to being even in $v_{\|}$. As mention in reference [36], we have $\sum_i q_i\int\mathrm{d}\mu\mathrm{d}\varepsilon F_{\mathrm{g1}}\left(\psi,\mu,\varepsilon\right)=g'$. Therefore, both equation (B.2) and equation (B.10) describe the Pfirsch-Schlüter current in collisionless process. In our code, the distribution f is decomposed into an equilibrium part $f_0=n_0\left(\boldsymbol{X}\right)f_{\mathrm{M}}$ and a perturbed part δf ($=F_{\mathrm{g1}}$). The Pfirsch-Schlüter current ($J_{\mathrm{ps}}=J_{\|}$) can be calculated in collisionless process.

References

[1] Qu W X and Callen J D 1985 Nonlinear growth of a single neoclassical MHD tearing mode in a tokamak Madison: University of Wisconsin
[2] Carrera R, Hazeltine R D and Kotschenreuther M 1986 *Phys. Fluids* **29** 899
[3] Chang Z *et al* 1995 *Phys. Rev. Lett.* **74** 4663
[4] La Haye R J 2006 *Phys. Plasmas* **13** 055501
[5] Igochine V 2015 *Active Control of Magneto-Hydrodynamic Instabilities in Hot Plasmas* (Berlin, Heidelberg: Springer)
[6] Lütjens H, Luciani J F and Garbet X 2001 *Phys. Plasmas* **8** 4267
[7] Muraglia M *et al* 2009 *Nucl. Fusion* **49** 055016
[8] Cai H S 2019 *Nucl. Fusion* **59** 026009
[9] Cai H S *et al* 2011 *Phys. Rev. Lett.* **106** 075002
[10] Ishizawa A *et al* 2021 *Nucl. Fusion* **61** 114002
[11] Maget P *et al* 2010 *Nucl. Fusion* **50** 045004
[12] Muraglia M *et al* 2017 *Nucl. Fusion* **57** 072010
[13] Maget P *et al* 2016 *Nucl. Fusion* **56** 086004
[14] Wei L *et al* 2016 *Nucl. Fusion* **56** 106015
[15] Widmer F *et al* 2019 *Nucl. Fusion* **59** 106012
[16] Yu Q 2020 *Nucl. Fusion* **60** 084001
[17] Wang Z X, Wei L and Yu F 2015 *Nucl. Fusion* **55** 043005
[18] Poli E *et al* 2003 *Plasma Phys. Control. Fusion* **45** 71
[19] Imada K *et al* 2019 *Nucl. Fusion* **59** 046016
[20] Lin Z, Tang W M and Lee W W 1995 *Phys. Plasmas* **2** 2975
[21] Kim K *et al* 2012 *Phys. Plasmas* **19** 082503
[22] Sasinowski M and Boozer A H 1995 *Phys. Plasmas* **2** 610
[23] Sasinowski M and Boozer A H 1997 *Phys. Plasmas* **4** 3509
[24] Poli E *et al* 2002 *Phys. Rev. Lett.* **88** 075001
[25] Wang F *et al* 2019 *Phys. Plasmas* **26** 052516
[26] Dong G and Lin Z 2017 *Nucl. Fusion* **57** 036009
[27] Suzuki Y *et al* 2013 *Plasma Phys. Control. Fusion* **55** 124042
[28] Liu Y W *et al* 2005 *Plasma Sci. Technol.* **7** 2801
[29] Fu G Y *et al* 2006 *Phys. Plasmas* **13** 052517
[30] Todo Y and Sato T 1998 *Phys. Plasmas* **5** 1321
[31] Zhang H W *et al* 2022 *Nucl. Fusion* **62** 026047
[32] Wang S and Ma Z W 2015 *Phys. Plasmas* **22** 122504.
[33] Zhang W *et al* 2021 *Comput. Phys. Commun.* **269** 108134
[34] Cary J R and Brizard A J 2009 *Rev. Mod. Phys.* **81** 693
[35] Boozer A H and Kuo-Petravic G 1981 *Phys. Fluids* **24** 851
[36] Zheng L J 2015 *Advanced Tokamak Stability Theory* (San Rafael: Morgan & Claypool Publishers)
[37] Zhang H W *et al* 2019 *Int. J. Comput. Fluid Dyn.* **33** 393

[38] Choi M J *et al* 2014 *Nucl. Fusion* **54** 083010
[39] Hinton F L and Hazeltine R D 1976 *Rev. Mod. Phys.* **48** 239
[40] Sauter O, Angioni C and Lin-Liu Y R 1999 *Phys. Plasmas* **6** 2834
[41] Redl A *et al* 2021 *Phys. Plasmas* **28** 022502
[42] Hager R and Chang C S 2016 *Phys. Plasmas* **23** 042503
[43] Hegna C C and Callen J D 1994 *Phys. Plasmas* **26** 2308
[44] Wilson H R *et al* 1996 *Phys. Plasmas* **3** 248
[45] Yu Q Q and Günter S 1998 *Plasma Phys. Control. Fusion* **40** 1989
[46] Yu Q, Günter S and Lackner K 2004 *Phys. Plasmas* **11** 140
[47] Hastie R J, Militello F and Porcelli F 2005 *Phys. Rev. Lett.* **95** 065001